Generalized Phase Diagrams for Graphene CVD growth on Cu(111)

Tongtong Wang(王彤彤)[1,2], Ke Jin(金柯)[1,2], Yishi Zhang(张倚石)[1,2], and Dajun Shu(舒大军)[1,2*]

[1] National Laboratory of Solid State Microstructures and School of Physics,
Nanjing University, Nanjing 210093, China

[2]Collaborative Innovation Center of Advanced Microstructures, Nanjing 210093, China

August 20, 2026

Abstract

Understanding the competition between first-layer lateral expansion and second-layer nucleation is essential for layer-controlled graphene growth via chemical vapor deposition (CVD). Here, we develop a generalized phase-diagram framework that incorporates two key effects often neglected in existing growth models: substrate strain induced by thermal expansion and chemical desorption arising from reverse dehydrogenation. Combining first-principles calculations with rate-equation theory, we map the complex multi-step CVD process onto an effective quasi-physical vapor deposition description and establish generalized growth phase diagrams. The resulting diagrams reveal that tensile strain expands the bilayer graphene (BLG) growth window for critical nucleus sizes $i^* > 1$, whereas chemical desorption suppresses BLG formation under low deposition fluxes. By directly connecting experimentally controllable variables, including temperature, hydrogen pressure, and substrate strain, to graphene layer selectivity, this framework provides a predictive guide for rational synthesis of high-quality uniform single- or bilayer graphene and offers practical parameter-tuning strategies for graphene-based nanomaterials.

Keywords: Bilayer Graphene; CVD; Phase diagrams

PACS: 81.05.ue, 81.15.Gh, 61.48.Gh

1. Introduction

Graphene continues to attract intense research interest due to its extraordinary electronic, optical, mechanical, and thermal properties [1–6]. While single-layer graphene (SLG) has laid the foundation for 2D materials research, bilayer graphene (BLG) exhibits unique properties depending on its layer stacking. Specifically, AB-stacked BLG exhibits a tunable band gap in a vertical electric field, while twisted BLG hosts novel correlated states such as Mott insulating state and superconductivity [7–11]. Chemical vapor deposition (CVD) on copper substrate has emerged as the most viable approach for the scalable production of high-quality graphene [12,13]. Unintended adlayer formation can degrade carrier mobility and impede device integration, highlighting the need for strategies to guide layer-selective growth [14,15], highlighting the need for strategies to achieve precise control over layer number.

The CVD growth of graphene on catalytic surfaces is a complex multi-stage process, encompassing the decomposition of gas-phase precursors (typically CH_4), surface diffusion of carbon monomers, nucleation, and subsequent island

*Corresponding author. E-mail: djshu@nju.edu.cn

growth. Extensive theoretical investigations have elucidated many of these aspects, with particular focus on precursor dissociation and surface kinetics. For CH_4 decomposition on Cu substrates, the catalytic pathways and the dominant growth species have been characterized in detail through first-principles calculations [16–20]. Regarding growth kinetics, multiscale modeling has highlighted the critical role of surface kinetics in governing the growth rate and morphology [21–28]. In the context of BLG, the self-limiting mechanism leads to a characteristic "inverse wedding cake" growth mode, where the competition between first-layer expansion and second-layer nucleation becomes the decisive factor [29–34].

In our previous work, we developed a rate-equation model to capture this competition by reducing complex surface kinetics into two dimensionless parameters, α, characterizing the competition between edge-crossing and attachment, and Γ, representing the relative rate of surface diffusion with respect to the deposition flux [35]. Within this framework, a phase diagram was constructed to map out the SLG and BLG growth regimes, successfully elucidating the role of hydrogen pressure.

However, two important physical effects were omitted for simplicity in our previous framework. First, temperature can indirectly influence graphene growth through thermal-expansion-induced substrate strain, which modifies both surface kinetics and cluster formation energetics [36–39]. Second, chemical desorption via reverse dehydrogenation reactions (*i.e.*, reassociation of adsorbed C and H into hydrocarbon species) can deplete surface carbon monomers under high hydrogen partial pressure [40–43]. Consequently, the coupled influence of thermal strain and chemical desorption on the kinetic parameters remains unexplored. Beyond that, recent study found that high hydrogen partial pressure shifts the nucleation balance, where hydrogen stabilizes small carbon rings in the nucleation process [44]. Furthermore, a "sunk growth" mode was proposed where the second layer partially embeds into the Cu surface [45–47]. These reports highlight the complexity of graphene growth on Cu. To understand these complex growth mechanisms, the first essential step is to construct a unified physical picture of growth phase diagram that can integrate the H2-involved reversible decomposition and the temperature-dependent surface kinetics.

In this work, we extend our previous rate-equation framework to simultaneously account for strain-modulated kinetics and chemical desorption of carbon monomers. Through systematic first-principles calculations, we evaluate the kinetic barriers and cluster stabilities under biaxial strain. By introducing effective deposition and desorption rates (F_{eff} and z_{eff}), the multi-step CVD process is transformed into an effective quasi-PVD process. We establish a generalized kinetic framework for layer-selective graphene growth, in which the competition between first-layer expansion and second-layer nucleation is characterized by the coupled effects of α, Γ, and the newly introduced desorption parameter Z. Within this framework, we further show that tensile-strained Cu(111) favors BLG growth for critical nucleus sizes $i^* > 1$. Chemical desorption further modifies the phase boundary in the high-Γ regime through the additional kinetic suppression introduced by the parameter Z. These findings establish a robust theoretical foundation for the rational design of CVD parameters to synthesize high-quality single-layer or bilayer graphene.

2. Computational Details

Following our previous work, graphene growth on Cu(111) is described using a coarse-grained kinetic framework in which carbon monomers are treated as the dominant growth species, which is valid under low H_2 pressure. To distinguish the kinetic environments associated with different graphene layers, the Cu surface is divided into exposed and covered substrate regions depending on the presence of overlying graphene islands. Kinetic processes occurring on the exposed substrate are defined as first-layer events (denoted by subscript surf), whereas processes taking place beneath graphene

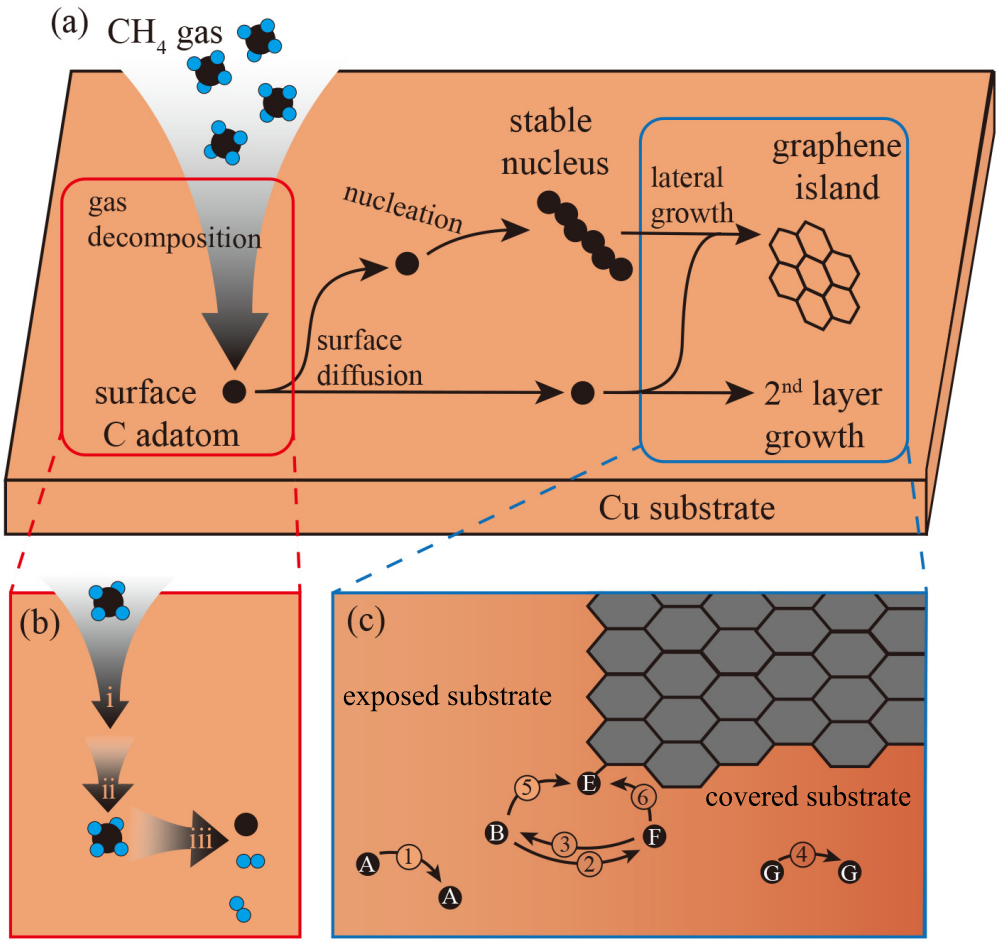


Figure 1: (a) Schematic diagram of all processes involved in graphene growth. The red rectangle highlights the decomposition reaction process, while the blue rectangle highlights the surface growth process. (b) Detailed view of the gas reaction processes, consisting of three steps. (c) Detailed view of the surface growth processes. Six processes are considered in this model.

islands correspond to second-layer events (denoted by subscript gap).

Figure 1(a) summarizes the kinetic processes involved in graphene CVD growth, which are separated into two coupled stages, namely the *precursor decomposition stage* (red box) and the *surface growth stage* (blue box). As illustrated in Fig. 1(b), the precursor decomposition stage includes (i) gas-phase transport of CH_4, (ii) transport across the vapor–substrate interface, and (iii) sequential dehydrogenation reactions that generate surface carbon monomers and H_2. The carbon monomers subsequently participate in the surface growth stage shown in Fig. 1(c). This stage encompasses several elementary pathways: monomer diffusion on the exposed substrate (A $\leftrightarrow$ A, process no. 1), edge crossing between exposed and covered substrate regions (B $\leftrightarrow$ F, processes no. 2 and no. 3), monomer diffusion beneath the graphene island (G $\leftrightarrow$ G, process no. 4), and monomer attachment to the graphene edge from either the exposed substrate (B $\rightarrow$ E, process no. 5) or the covered substrate (F $\rightarrow$ E, process no. 6).

As shown in Fig. S1 of the Supporting Information, a metastable site M exists beneath the graphene island edge and acts as an intermediate state connecting sites B and F. Consequently, edge attachment can proceed through both direct pathways and indirect pathways involving the metastable site M. To incorporate these coupled edge-transfer processes into an effective kinetic description, we employ a star–delta (Y–Δ) transformation adapted from electrical circuit theory,

as illustrated in the inset of Fig. S1. By assuming the coverage of metastable site M achieves steady state, the effective hopping rates are obtained as

$$\begin{aligned} \nu_2 &= \frac{\nu_{\mathrm{BM}}\nu_{\mathrm{MF}}}{\nu_{\text{M-tot}}}, \quad \nu_5 = \frac{\nu_{\mathrm{BM}}\nu_{\mathrm{ME}}}{\nu_{\text{M-tot}}} + \nu_{\mathrm{BE}}, \\ \nu_3 &= \frac{\nu_{\mathrm{FM}}\nu_{\mathrm{MB}}}{\nu_{\text{M-tot}}}, \quad \nu_6 = \frac{\nu_{\mathrm{FM}}\nu_{\mathrm{ME}}}{\nu_{\text{M-tot}}} + \nu_{\mathrm{FE}}, \end{aligned} \tag{1}$$

where $\nu_{\text{M-tot}} = \nu_{\mathrm{MB}} + \nu_{\mathrm{MF}} + \nu_{\mathrm{ME}}$. The hopping rate of the elementary process from site i to j is calculated by $\nu_{ij} = \nu_0 \exp(-\beta \Delta G_{ij})$ with $\beta = (k_B T)^{-1}$.

To investigate strain effects, a uniform biaxial strain $\varepsilon = (a - a_0)/a_0$ is applied to the Cu(111) slab, where $a_0 =$ 3.634 Å is the optimized lattice constant of bulk Cu at 0 K. Both tensile and compressive strain up to 2% are considered. All structural models employed in the calculations are identical to those established in our previous work [35].

All calculations are performed based on density functional theory (DFT) in the Perdew-Burke-Ernzerhof generalized gradient approximation (GGA-PBE) [48] using the Vienna Ab initio Simulation Package (VASP) [49,50], with Projector-Augmented Wave (PAW) methods [51]. The semiempirical approach DFT-D2 is used to include the van der Waals (vdW) interactions [52]. Additional PBE-D3 benchmark calculations yield consistent results with PBE-D2, as shown in Table S1 and Fig. S2 in the Supporting Information. A cutoff energy of 650 eV for the plane wave basis set is employed for all calculations. The in-plane Brillon zones of models are sampled by a Γ-centered k-point mesh to guarantee the convergence [53]. The relaxations are carried out until forces on the free atoms are converged to 0.01 eV/Å for structural optimizations. The energy barriers of the kinetic processes are calculated by the climbing image nudged elastic band (CI-NEB) method with the forces on the free atoms converged to 0.02 eV/Å [54]. These settings ensure a convergence in total energy of 0.1 meV/atom.

3. Results and Discussion

3.1. Strain-Dependent Energetics and Kinetics

The growth mode of graphene is governed by the competition between first-layer lateral expansion and second-layer nucleation. To establish how substrate strain modifies this competition, we systematically investigate both the thermodynamic and kinetic aspects of graphene growth on Cu(111). Thermodynamically, strain-dependent growth driving forces and cluster formation energies are evaluated to characterize the nucleation barriers. Kinetically, the strain dependence of surface diffusion and attachment processes is analyzed to determine how it modifies carbon monomer transport. Together, these thermodynamic and kinetic effects underpin the generalized growth phase diagram.

3.1.1. Thermodynamic Analysis: Growth Driving Forces and Nucleation Barriers

The thermodynamic driving force for graphene growth is determined by the carbon supersaturation, defined as the chemical potential difference between surface carbon monomers and graphene on the same substrate, $\Delta\mu = \mu_{\text{monomer}} - \mu_{\text{gr}}$, where the monomer chemical potential is given by $\mu_{\text{monomer}} = \mu_{\mathrm{CH_4}} - 2\mu_{\mathrm{H_2}}$. Within the ideal-gas approximation, the supersaturation can be expressed as $\Delta\mu = \Delta\mu^{\ominus}(T) - kT \ln \frac{(P_{\mathrm{H_2}})^2}{P^{\ominus} P_{\mathrm{CH_4}}}$, where $\Delta\mu^{\ominus}(T) = \mu^{\ominus}_{\mathrm{CH_4}} - 2\mu^{\ominus}_{\mathrm{H_2}} - \mu_{\text{gr}}$ represents the supersaturation under the standard pressure $P^{\ominus} = 1$ bar. The temperature dependence of $\Delta\mu^{\ominus}(T)$ can be further decomposed into enthalpic and entropic contributions according to $\Delta\mu^{\ominus}(T) = \Delta h^{\ominus} - T\Delta s^{\ominus}$. Using the experimentally

determined values $\Delta h^{\ominus} = 0.9515$ eV and $\Delta s^{\ominus} = 1.119 \times 10^{-3}$ eV/K for graphene growth on Cu [55], the supersaturation can be evaluated as a function of the experimental parameters $t = P_{H_2}/P^{\ominus}$ and $w = P_{H_2}/P_{CH_4}$. As summarized in Table S2 and illustrated in Fig. S3, $\Delta\mu$ can reach values as high as ~ 1.5 eV at low $t \times w$ [56,57]. Increasing $t \times w$ monotonically reduces the supersaturation and eventually drives the system into the etching regime with $\Delta\mu < 0$ [58]. Note that the chemical potential of carbon atom in graphene on Cu substrate is expected to become higher at enhanced temperature due to the increasing lattice mismatch between graphene and Cu substrate, which leads to a smaller driving force for the same partial pressure conditions than in graphite.

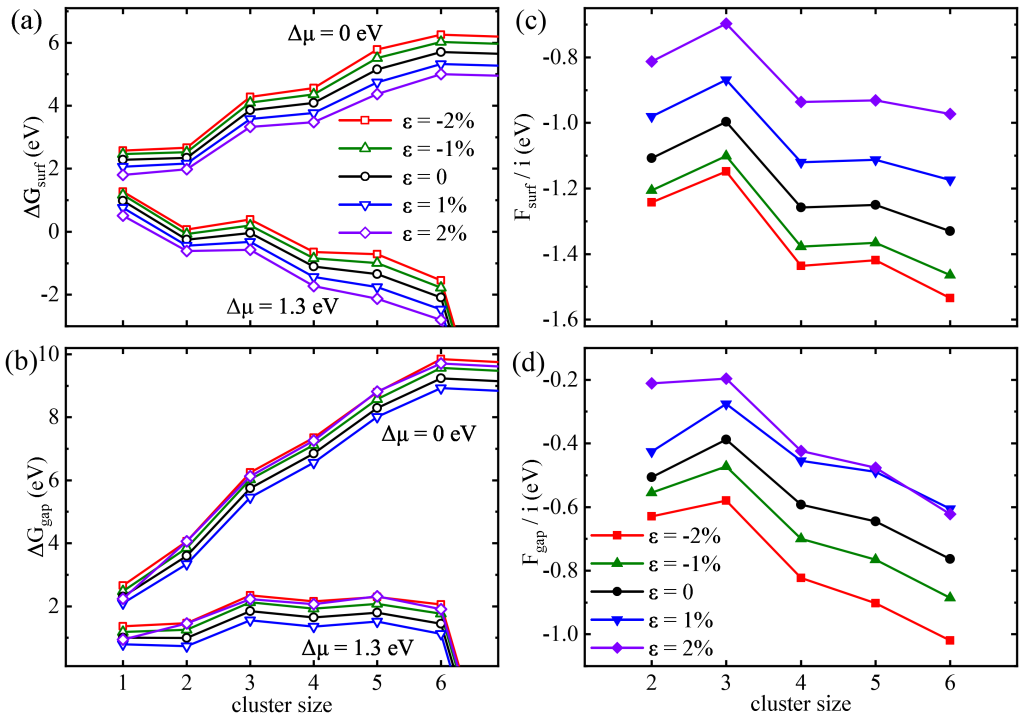


Figure 2: The formation works of C clusters (a) on the exposed substrate and (b) at the graphene-substrate gap under different strains. The free energy change per C atom for C cluster formation (c) on the exposed substrate and (d) at the graphene-substrate gap under different strains.

Beyond the thermodynamic driving force, we next examine the formation of carbon clusters and the associated nucleation behavior. The formation work of a carbon cluster C_i containing i atoms is defined as $\Delta G(i,T) = E_a(i) - k_B T \ln q_i - i(\mu_{gr} + \Delta\mu)$, where $E_a(i) = E_{tot}(i) - E_{sub}$ is the energy difference between cluster-adsorbed substrate and bare substrate, and q_i is the partition function of the cluster confined within a single adsorption site. According to the critical condition $\partial\Delta G(i)/\partial i|_{i=i^*} = 0$ in classical nucleation theory, the critical size i^* generally decreases with increasing $\Delta\mu$. In the present work, the cluster partition-function contribution is neglected for simplicity, thus $\Delta G(i) \approx E_a(i) - iE_{gr} - i\Delta\mu$, where E_{gr} is the energy per carbon atom in graphene on the same substrate. The justification of this approximation is assessed by evaluating the local harmonic vibrational contribution, as shown in Fig. S4 of the Supporting Information.

Thermodynamically, previous DFT calculations showed that the chain structure is more favorable on Cu(111) for C_1 to C_{13} [59,60]. Kinetically, the barrier of C_6 ring breaking into C_6 chain is approximately 0.66 eV, suggesting that this conversion is thermally accessible at typical graphene growth temperature [60]. Therefore, we use the chain configurations for C_1–C_6 clusters to address the initial nucleation process under relatively low H_2 pressure. Using the most stable linear

configurations of C_i clusters (i = 1–6), we calculate the formation work on both the exposed substrate (ΔG_{surf}) and in the graphene–substrate gap (ΔG_{gap}), as shown in Fig. 2(a,b). For all cluster sizes considered here, ΔG_{surf} remains lower than ΔG_{gap}, indicating that first-layer nucleation is thermodynamically more favorable than second-layer nucleation. This energetic preference is further reflected in the corresponding critical nucleus sizes. For $\Delta\mu = 1.3$ eV, the critical nucleus size is $i^* = 1$ for first-layer nucleation but increases to $i^* = 3$ for second-layer nucleation. The strain dependence of $\Delta G(i)$ further reveals distinct responses for the two growth layers. On the exposed Cu surface, $\Delta G_{\mathrm{surf}}(i)$ generally decreases under tensile strain, indicating an enhanced thermodynamic driving force for first-layer nucleation. In contrast, the strain dependence of $\Delta G_{\mathrm{gap}}(i)$ exhibits a notable anomaly under 2% tensile strain. This behavior is likely associated with the reduced graphene–substrate interfacial spacing induced by strong tensile deformation.

According to classical nucleation theory [61], the equilibrium coverage of an i-atom cluster is given by $\theta_{C_i} = \exp[-\beta\Delta G(i)]$, while the monomer coverage satisfies $\theta_C = \exp[-\beta\Delta G(1)]$. The cluster coverage can therefore be rewritten as $\theta_{C_i} = (\theta_C)^i \exp[-\beta F(i)]$, where $F(i) = \Delta G(i) - i\Delta G(1)$ is the free energy cost of forming a cluster C_i from i surface monomers. Since $F(i)$ directly governs the equilibrium cluster population and the steady-state nucleation rate, we further analyze the strain dependence of the formation energy per atom, $F(i)/i$ for cluster size of i = 1–6. The corresponding results for first-layer clusters (F_{surf}/i) and second-layer clusters (F_{gap}/i) are shown in Fig. 2(c) and (d), respectively. For simplicity, entropic contributions are again neglected, yielding $F(i) = \Delta E_a(i) - i\Delta E_a(1)$.

The calculated formation energies indicate a clear energetic preference for first-layer nucleation over second-layer nucleation. Specifically, F_{surf} remains consistently lower than F_{gap}, indicating that cluster formation on the exposed Cu surface is thermodynamically more favorable than beneath the graphene overlayer. Overall, both F_{surf}/i and F_{gap}/i generally decrease with increasing cluster size, reflecting the enhanced stability of larger carbon clusters. A notable exception occurs for the dimer, whose formation energy per atom is lower than that of the trimer owing to the exceptionally strong C–C covalent bonding within the dimer configuration. In addition, both F_{surf} and F_{gap} decrease under compressive strain, suggesting that compressive strain favors cluster nucleation.

Since $\Delta G(i)$ and $F(i)$ are referenced to E_{gr} and $E_a(1)$, respectively, the opposite strain dependences of $\Delta G(i)$ and $F(i)$ indicate a size-dependent response of $E_a(i)$ to substrate strain. Indeed, for clusters with size i = 1–6, $E_a(i)$ decreases monotonically with increasing tensile strain, while the magnitude of this reduction becomes weaker for larger clusters. In graphene, however, the energy per carbon atom E_{gr} increases under tensile strain. This contrasting size dependence originates from the competition between two opposing effects: tensile strain strengthens the interaction between carbon clusters and the Cu substrate, while simultaneously inducing substantial deformation of the C–C bonding network, which destabilizes carbon aggregation.

3.1.2. Kinetic Processes: Surface Diffusion and Attachment Dynamics

As illustrated schematically in Fig. 1, both the precursor decomposition stage and the surface growth stage involve multiple thermally activated elementary processes. Because methane decomposition occurs locally at individual adsorption sites, the associated reaction barriers are expected to exhibit only weak sensitivity to substrate strain. In contrast, the surface growth stage involves long-range monomer transport and edge attachment processes that are intrinsically coupled to the substrate lattice geometry. We therefore focus here on the strain dependence of the surface diffusion and attachment kinetics that govern graphene growth.

The NEB energy profiles of the elementary hopping processes are shown in Fig. S5 for both unstrained Cu(111) and

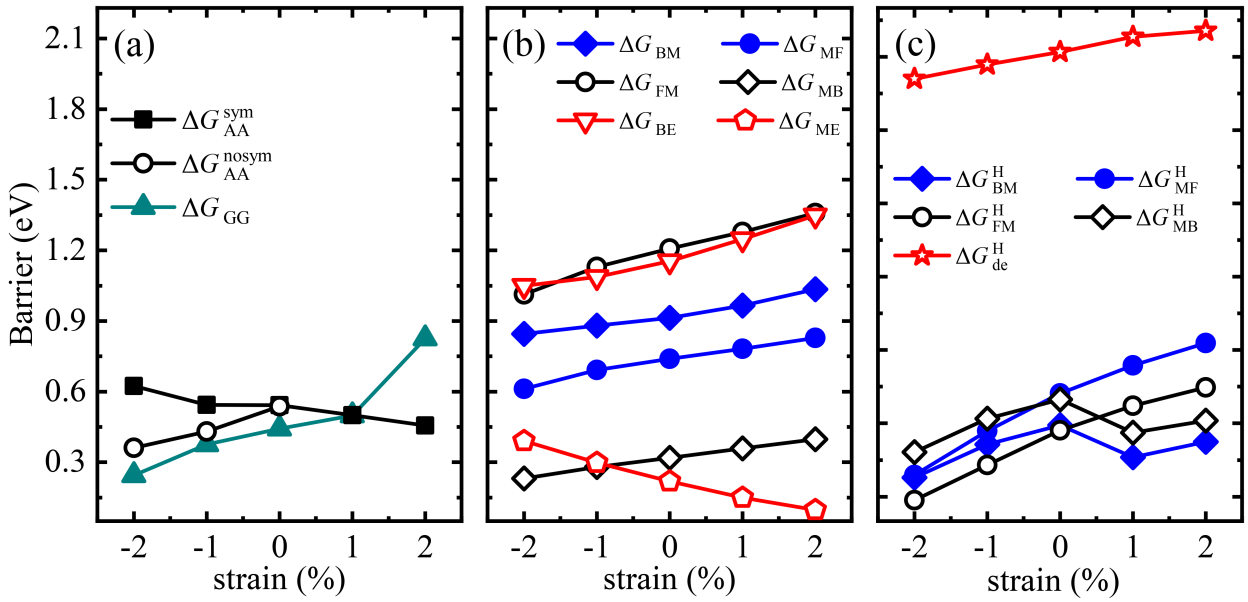


Figure 3: The change in surface process barriers under different strains. (a) The surface diffusion processes far away from the graphene island edges. (b) The surface diffusion processes across the pristine island edges and the attachment process to the pristine edges. (c) The surface diffusion processes across the H-terminated island edges and the H detachment process from the H-terminated edges.

that under a representative tensile strain of 2%. The most striking result is that the minimum energy pathway for diffusion on the exposed substrate (process no. 1) is altered under tensile strain. As shown in Fig. S6, when compressive strain is applied, the optimal pathway hopping between two equilibrium fcc sites is nearly parallel to the [111] direction, denoted as the "nosym" pathway. Under tensile strain, however, the pathway relaxes to a high-symmetry path, where the saddle point resides precisely above an hcp site, denoted as the "sym" pathway.

The activation barriers for all the elementary kinetic processes were systematically calculated under four strain conditions (-2%, -1%, 1%, and 2%), with the results summarized in Fig. 3(a) and (b). The two diffusion pathways associated with process no. 1 exhibit opposite strain dependences. Compressive strain reduces ΔG_{AA}^{nosym} but enhances ΔG_{AA}^{sym}, thereby rendering the "nosym" pathway kinetically preferred. Under tensile strain, the "nosym" pathway is unstable and the "sym" pathway becomes dominant. Consequently, the diffusion barrier on the exposed substrate, ΔG_{AA}, decreases under both compressive and tensile strain, irrespective of the strain sign. For diffusion across the island edge or beneath the island, the "nosym" pathway remains energetically favored across the entire strain range considered here. Therefore, the activation barriers of these processes (B $\leftrightarrow$ M $\leftrightarrow$ F, G $\leftrightarrow$ G) are reduced by compressive strain and raised by tensile strain. The direct attachment from the exposed substrate to the edge (B $\rightarrow$ E) also follows a similar trend, but the attachment barrier from the metastable site M displays an opposite trend that decreases with increasing strain. For the direct attachment from covered substrate to the edge (F$\rightarrow$E), we have constructed several reasonable direct pathways to start the NEB searching. However, all the attempts failed to yield a stable pathway circumventing the metastable M. As illustrated in Fig. S7, to realize this direct pathway, the C adatom must first move toward the graphene–substrate interface and then traverse the region between the bent graphene edge and the Cu substrate, where the available migration space is strongly restricted. We therefore set ν_{FE} as zero due to the steric blocking of the graphene edge.

For comparison, we also consider the influence of hydrogen termination at the island edges on these kinetics, which

is experimentally relevant under high H_2 partial pressures. As shown in Fig. 3(c), hydrogen-terminated edges evidently reduce the barriers for edge crossing. Similar to the H-free case, these barriers generally increase under tensile strain and decrease under compressive strain. A notable difference is that the strain dependence becomes non-monotonic as the system evolves from compressive to tensile strain for $\Delta G^{\mathrm{H}}_{\mathrm{BM}}$ and $\Delta G^{\mathrm{H}}_{\mathrm{MB}}$. This behavior originates from a strain-induced change in the B↔M migration pathway. Hydrogen termination suppresses the downward bending of the graphene edge, leaving the B↔M migration region relatively weakly affected by the overlying graphene and thereby allowing pathway competition similar to that on bare Cu(111). The converged pathway changes from the non-symmetrical one at $\varepsilon = -1\%$ to the symmetrical one at $\varepsilon = 0\%$, accounting for the non-monotonic behavior in Fig. 3(c), as shown in Fig. S8 in the Supporting Information. Meanwhile, hydrogen termination strongly suppresses edge attachment because the hydrogen detachment barrier $\Delta G^{\mathrm{H}}_{\mathrm{de}}$ (~ 2 eV) is substantially higher than both ΔG_{BE} and ΔG_{ME}.

3.2. Enhanced Rate-Equation Framework

3.2.1. Gas-phase reactions: from CVD to quasi-PVD

To establish a tractable rate-equation description of graphene CVD growth, the complex multistep precursor reaction is transformed into effective deposition and desorption processes. Within this treatment, the overall CVD growth can be mapped onto an effective quasi-PVD framework. The decomposition of methane (CH_4) precursors occurs through either direct gas-phase dissociation or catalytic dehydrogenation on the Cu surface following adsorption. In both situations, the decomposition process is modeled as a sequence of four elementary dehydrogenation steps. Specifically, the elementary steps and the overall reactions of CH_4 decomposition on Cu are as follows,

$$\mathrm{CH}_{4-l}(\mathrm{a}) + \mathbb{A} \rightleftharpoons \mathrm{CH}_{3-l}(\mathrm{a}) + \mathrm{H}(\mathrm{a}), \quad (l = 0,1,2,3) \tag{R1}$$

$$\mathrm{CH}_4(\mathrm{a}) + 4\,\mathbb{A} \rightleftharpoons \mathrm{C}(\mathrm{a}) + 4\,\mathrm{H}(\mathrm{a}). \tag{R2}$$

Here $\mathbb{A}$ denotes an empty adsorption site of the Cu substrate and (a) indicates the adsorbed state. The kinetics of the $(l+1)$-th dehydrogenation step (R1) are characterized by the forward and backward rate constants, denoted as k_l^+ and k_{l+1}^-, respectively. Meanwhile, the adsorption and desorption rate constants of CH_{4-l} ($l = 0,1,2,3$) are denoted as f_l and z_l. Accordingly, the surface density of the intermediate CH_{4-l}, denoted as θ_l, follows the evolution equation $\partial_t \theta_l = (P_l f_l \theta_{\mathbb{A}} - z_l \theta_l) + (\theta_{l-1} k_{l-1}^+ \theta_{\mathbb{A}} - \theta_l k_l^- \theta_{\mathrm{H}}) - (\theta_l k_l^+ \theta_{\mathbb{A}} - \theta_{l+1} k_{l+1}^- \theta_{\mathrm{H}})$. Here P_l represents the partial pressure of the gas-phase species, while $\theta_{\mathbb{A}}$ and θ_{H} denote the densities of empty adsorption sites and adsorbed hydrogen atoms on the substrate, respectively. Under typical CVD conditions, the first term (direct adsorption and desorption) of the evolution equation is negligible compared with the other two terms (dehydrogenation flux). Therefore, assuming the dehydrogenation steps reach steady state yields an expression for the effective decomposition rate k_d^+ of CH_4 in the overall reaction (R2),

$$\frac{1}{\theta_{\mathbb{A}}^3 k_d^+} = \frac{1}{k_0^+} + \sum_{i=1}^{3} \frac{1}{K_{0i} k_i^+}, \quad K_{0i} = \prod_{l=0}^{i-1} \frac{k_l^+ \theta_{\mathbb{A}}}{k_{l+1}^- \theta_{\mathrm{H}}}. \tag{2}$$

Similarly, the effective backward rate constant of (R2) is given by $k_d^- = K_{04} k_d^+ \theta_{\mathbb{A}}^4 / \theta_{\mathrm{H}}^4$, where K_{04} is defined analogously to the K_{0i} above. The resulting effective rate constants k_d^+ and k_d^- therefore represent the net methane decomposition flux after coarse-graining over the intermediate hydrocarbon species.

Further assuming that the surface coverage of CH_4 reaches a steady state via the overall decomposition reaction (R2) much faster than the growth timescale of carbon islands, the multistep CVD chemistry can be reduced to an effective rate

equation governing the surface concentration of carbon monomers, coverage θ_C,

$$\frac{d\theta_C}{dt} = F_{\text{eff}}\theta_{\mathbb{A}} - (k_g + z_{\text{eff}})\theta_C, \tag{3}$$

where k_g denotes the effective consumption rate constant of carbon monomers due to nucleation and island growth, as will be specified later. These steady-state approximations are appropriate under the high-temperature CVD conditions considered here, where dehydrogenation is much faster than graphene island growth. Increasing P_{H_2} modifies the backward dehydrogenation rates and hence the steady-state intermediate coverages, rather than the steady-state treatment itself. Consequently, the effective deposition flux F_{eff} and the effective desorption rate constant z_{eff} of carbon monomers are given as follows,

$$F_{\text{eff}} = P_C f_C + \frac{P_{CH_4} f_{CH_4} k_d^+ \theta_{\mathbb{A}}^4}{z_{CH_4} + k_d^+ \theta_{\mathbb{A}}^4}, \tag{4}$$

$$z_{\text{eff}} = z_C + \frac{z_{CH_4} k_d^- \theta_H^4}{z_{CH_4} + k_d^+ \theta_{\mathbb{A}}^4}. \tag{5}$$

The first term in F_{eff} accounts for direct impingement of C atoms (negligible under typical CVD conditions), and the second term represents the net supply from CH_4 decomposition. Similarly, the desorption rate z_{eff} contains a physical desorption term z_C (usually very small due to the strong chemisorption of carbon on Cu) and a chemical desorption term arising from the reverse dehydrogenation in (R2). z_{eff} is dominated by the reverse dehydrogenation term at high P_{H_2}. This chemical desorption pathway, analogous to the mechanism quantified by Vlassiouk *et al.* [40], effectively depletes carbon monomers and reduces their steady-state concentration. Therefore, z_{eff} represents an effective non-growth depletion for carbon monomers. In this quasi-PVD framework, Eq. (3) is analogous to a PVD rate equation but with renormalized deposition and desorption rates that incorporate chemical reactions.

3.2.2. First-layer nucleation and growth

Based on classical nucleation theory [62,63], first-layer clusters are treated as stable islands only when their size n exceeds a critical value i^*, otherwise, they remain as unstable embryos. Assuming a steady-state formation current for embryos of sizes up to $n \leq i^*$, we obtain the steady-state nucleation rate

$$J_{\text{nuc}}(i^*) = w_{i^*}^+ \theta_C^{i^*+1} \exp[-\beta F_{\text{surf}}(i^*)], \tag{6}$$

where $w_{i^*}^+ = \sigma_{i^*}\nu_1$ is the forward reaction rate constant for the attachment process $C + C_{i^*} \rightleftharpoons C_{i^*+1}$, with σ_{i^*} the capture number of critical nucleus, and $\nu_1 = \nu_{AA}$ the rate of process no. 1 (diffusion of carbon monomers on the exposed substrate).

By grouping all stable islands of size $n > i^*$ together, with a total density of first-layer stable islands θ_{isl}, an average capture number σ_s and an average attachment rate to the island edge $w_s^+ = \sigma_s\nu_1$, the total monomer flux toward these stable islands is given by $J_{\text{isl}} = w_s^+ \theta_C \theta_{\text{isl}}$. The total consumption rate of C monomers, accounting for both nucleation and island growth, is thus defined as $k_g\theta_C = (i^*+1)J_{\text{nuc}} + J_{\text{isl}}$. In the growth regime, $k_g\theta_C \simeq J_{\text{isl}}$ since $(i^*+1)J_{\text{nuc}} \ll J_{\text{isl}}$.

If desorption is negligible ($z_{\text{eff}} \to 0$), the monomer population is governed solely by the competition between deposition and island capture, $\theta_C = F_{\text{eff}}\theta_{\mathbb{A}}/(\sigma_s\nu_1\theta_{\text{isl}})$, according to Eq. (3). This leads to the familiar PVD scaling for island density. In contrast to conventional PVD growth, graphene CVD involves an additional non-growth depletion pathway arising from chemical desorption. Consequently, the effective desorption rate z_{eff} must be retained explicitly in Eq. (3). Accounting for this depletion pathway, the steady-state monomer density is expressed as

$$\theta_C = F_{\text{eff}}\theta_{\mathbb{A}}/(\sigma_s\nu_1\theta_{\text{isl}} + z_{\text{eff}}). \tag{7}$$

Substituting Eq. (7) into (6), and then integrating the nucleation rate J_{nuc}, we obtain the saturation island density [35],

$$\theta_{\mathrm{isl}} = \left[B_{i^*}\Gamma^{-i^*} + Z^{i^*+2}\right]^{1/(i^*+2)} - Z, \tag{8}$$

where $B_{i^*} = \frac{(i^*+2)\sigma_i}{\sigma_s^{i^*+1}}\Theta_c \exp\left[-\beta F_{\mathrm{surf}}(i^*)\right]$, and

$$\Gamma = \nu_1/F_{\mathrm{eff}}, \quad Z = z_{\mathrm{eff}}/(\sigma_s \nu_1). \tag{9}$$

Here Θ_c is the coverage at which island saturation occurs. Within this generalized framework, Γ characterizes the competition between surface diffusion and deposition, while Z quantifies the relative strength of chemical desorption against island growth. Notice that when $Z = 0$, Eq. (8) reduces to the familiar PVD scaling $\theta_{\mathrm{isl}} \propto \Gamma^{-i^*/(i^*+2)}$.

3.2.3. Second-layer nucleation beneath islands

As first-layer graphene islands expand, carbon monomers on the exposed Cu substrate can diffuse across the island edges and accumulate in the graphene-substrate gap. The monomers in the gap serve as the precursor reservoir for second-layer nucleation. To distinguish the monomer populations on bare substrate and in the gap, we denote their respective concentrations as η_1 and η_2. With the effective deposition rate F_{eff}, the condition of mass conservation gives

$$\pi(L^2 - R^2)F_{\mathrm{eff}}\frac{\theta_{\mathrm{isl}}}{\theta_{\mathrm{isl}} + Z} = 2\pi R(\eta_1 \nu_5 + \eta_2 \nu_6), \tag{10}$$

where $L = 1/\sqrt{\pi\theta_{\mathrm{isl}}}$ is half the average island separation. The factor $\theta_{\mathrm{isl}}/(\theta_{\mathrm{isl}} + Z)$ accounts for the competition between island growth and monomer depletion through chemical desorption. Assuming a steady state for η_2 yields the kinetic relation $\eta_1 \nu_2 = \eta_2(\nu_3 + \nu_6)$. Substituting this relation into Eq. (10), we derive the monomer density beneath the island

$$\eta_2 = \frac{L^2 - R^2}{2R\alpha\Gamma}\frac{\theta_{\mathrm{isl}}}{\theta_{\mathrm{isl}} + Z}, \tag{11}$$

where α accounts for the competition between the kinetic processes,

$$\alpha = (\nu_3\nu_5 + \nu_2\nu_6 + \nu_5\nu_6)/(\nu_1\nu_2). \tag{12}$$

Here $\nu_{2,3,5,6}$ denote the effective kinetic rates obtained from the Y–Δ transformation in Eq. (1), while $\nu_1 = \nu_{\mathrm{AA}}$ and $\nu_4 = \nu_{\mathrm{GG}}$ correspond to monomer diffusion on the exposed and island-covered substrate, respectively.

Because no direct deposition occurs beneath the first-layer graphene islands, the confined monomer population rapidly reaches a spatially uniform concentration. The corresponding nucleation rate for a second-layer nucleus with critical size i^* is therefore $J_{\mathrm{gap}}(i^*) = \sigma_{i^*}\nu_4\eta_2^{i^*+1}\exp\left[-\beta F_{\mathrm{gap}}(i^*)\right]$, and the total number of second-layer nuclei that form before the first-layer islands coalesce (R reaches L) is

$$I_{\mathrm{gap}}(i^*) = \int_{R_n}^{L} J_{\mathrm{gap}}(i^*)\pi R^2 \frac{dt}{dR} dR, \tag{13}$$

where R_n represents the minimum radius at which second-layer nucleation can occur. This geometric threshold is associated with a 7-ring C_{24} cluster, corresponding to $R_n = 3$ in units of $\sqrt{A_0}$, where A_0 represents the area of a graphene unit cell. Substituting Eqs. (11) into the nucleation rate J_{gap}, and recognizing Eq. (10) as the growth rate $\partial_t(\pi R^2)$, we obtain

$$I_{\mathrm{gap}}(i^*) = \frac{C_{i^*}g_{i^*}(L)}{\alpha(2\alpha\Gamma)^{i^*}}\left(\frac{\theta_{\mathrm{isl}}}{\theta_{\mathrm{isl}} + Z}\right)^{i^*}, \tag{14}$$

where $C_{i^*} = \pi\lambda\sigma_{i^*}\exp\left[-\beta F_{\mathrm{gap}}(i^*)\right]$, $\lambda = \nu_4/\nu_1$, and $g_{i^*}(L) = \int_{R_n}^{L}(L^2 - R^2)^{i^*}R^{2-i^*}dR$.

The growth mode is determined by comparing $I_{\mathrm{gap}}(i^*)$ with unity. If $I_{\mathrm{gap}}(i^*) < 1$, no second-layer nucleus forms before island coalescence, resulting in SLG growth. Conversely, if $I_{\mathrm{gap}}(i^*) > 1$, second-layer nuclei can form prior to coalescence, thereby enabling BLG growth. The condition $I_{\mathrm{gap}}(i^*) = 1$ therefore defines the phase boundary in the (α, Γ) parameter space, with chemical desorption incorporated through the additional kinetic parameter Z.

3.3. The Phase Diagram Approach: Effects of Strain and Chemical Desorption on Graphene Growth

To establish a more realistic description of CVD growth, the phase diagram is generalized by incorporating the effects of substrate strain and chemical desorption. As discussed in Sec. 3, substrate strain strongly influences both cluster formation energetics and surface kinetics. During growth, such strain naturally arises from either lattice mismatch in epitaxial systems [64] or thermal expansion at elevated temperatures. In the present work, we focus on the latter mechanism, using temperature as an experimentally tunable parameter to indirectly modulate strain via the thermal expansion of the Cu substrate. The temperature-dependent tensile strain is determined from the thermal expansion of Cu relative to its lattice constant at 0 K. The diffusion barriers and cluster formation energies at finite temperature are then obtained by extrapolating the corresponding DFT results to the strain state associated with that temperature (see Figs. S9 and S10 for details). For an epitaxially constrained Cu film, the in-plane lattice parameter at the growth temperature is governed by the supporting substrate rather than by the free thermal expansion of Cu. Different epitaxial substrates therefore lead to different temperature-dependent strain states, which can modify both the SLG–BLG phase boundaries and the kinetic parameters (α, Γ) in the phase space.

The strain affects the growth phase behavior through two concurrent mechanisms: it both modifies the kinetic parameters α and Γ and shifts the phase boundary through strain-dependent cluster formation energies. In addition, chemical desorption introduces a finite parameter Z, providing an additional kinetic pathway for regulating graphene growth. In the following, we first analyze the temperature dependence of α, Γ, and Z, and then construct the generalized phase diagram. Finally, based on this framework, we discuss possible strategies for controlled BLG growth.

3.3.1. Variation of Parameters α, Γ and Z

To evaluate the kinetic parameters Γ and Z defined in Eq. (9), the surface coverages of vacancies ($\theta_{\mathbb{A}}$) and atomic hydrogen (θ_{H}) must first be determined. This is achieved by incorporating the adsorption and dissociation kinetics of hydrogen molecules together with reactions (R1) and (R2),

$$\mathrm{H_2(g)} + \mathbb{A} \rightleftharpoons \mathrm{H_2(a)}, \quad \mathrm{H_2(a)} + \mathbb{A} \rightleftharpoons \mathrm{2H(a)}. \tag{R3}$$

Here, $f_{\mathrm{H_2}}$ and $z_{\mathrm{H_2}}$ denote the adsorption and desorption rate constants of $\mathrm{H_2}$, while k_{H}^{+} and k_{H}^{-} represent the forward and backward rate constants for hydrogen dissociation on the substrate. The coverages of molecular hydrogen ($\theta_{\mathrm{H_2}}$) and atomic hydrogen (θ_{H}) are obtained from the steady-state conditions of reactions (R1)–(R3), while $\theta_{\mathbb{A}}$ satisfies the conservation constraint. In a typical CVD growth, the partial pressure of $\mathrm{H_2}$ is much larger than that of $\mathrm{CH_4}$, rendering the occupancy of hydrocarbon species (CH_i) negligible compared to hydrogen. Consequently, the site-conservation constraint simplifies to $\theta_{\mathrm{H_2}} + \theta_{\mathrm{H}} + \theta_{\mathbb{A}} \approx 1$. The hydrogen coverage θ_{H} is predominantly governed by the dissociative adsorption of $\mathrm{H_2}$. Under these steady-state conditions, the coverages are derived as $\theta_{\mathbb{A}} = \frac{1}{1+P_{\mathrm{H_2}} f_{\mathrm{H_2}}/z_{\mathrm{H_2}} + \sqrt{P_{\mathrm{H_2}} f_{\mathrm{H_2}} k_{\mathrm{H}}^{+}/(z_{\mathrm{H_2}} k_{\mathrm{H}}^{-})}}$ and $\theta_{\mathrm{H}} = \theta_{\mathbb{A}} \sqrt{P_{\mathrm{H_2}} f_{\mathrm{H_2}} k_{\mathrm{H}}^{+}/(z_{\mathrm{H_2}} k_{\mathrm{H}}^{-})}$.

According to the kinetic theory of gases, the deposition rate constant is given by $f = a^2(2\pi m k_B T)^{-1/2}$, where a^2 denotes the area of an adsorption site on the Cu(111) surface and m is the molecular mass. The partial pressure of gas-phase carbon monomers is assumed to be negligible, such that the first term in Eq. (4) can be omitted. Following transition state theory (TST), the rate constants for gas desorption (z) and surface reactions ($k^{\pm}$) are calculated by $(k_B T/h)\exp(-\beta\Delta G)$. The corresponding activation barriers (summarized in Table S3) are assumed to be strain-independent because of their localized nature.

Choosing a typical value of $P_{H_2} = 0.01\,\text{bar}$ and a gas ratio $w = 100$, the temperature dependences of α, Γ, and Z are illustrated in Fig. 4. The values of α are determined for both H-free and H-terminated graphene edges, representing the low and high P_{H_2} limits, respectively. The magnitude of α spans a wide range from approximately 10^{-7} to 10^{-1}, depending on whether the graphene island edges are hydrogen-passivated. Under intermediate hydrogen pressures, the island edges become partially hydrogenated. The resulting effective α falls between these two limits, smoothly shifting the system's operating point in the phase space rather than introducing an abrupt change in the SLG–BLG phase boundary.

While $\alpha_{\text{H-free}}$ remains relatively stable with a slight downward trend, α_{H} increases markedly with temperature. For the H-free system, the strain-induced enhancement of the effective barrier slightly outweighs the thermal activation effect as temperature increases, resulting in a weak decrease in $\alpha_{\text{H-free}}$. In contrast, hydrogen termination substantially modifies the surface kinetics, with enhanced ν_2^{H} and suppressed ν_5^{H} and ν_6^{H} relative to the H-free case. These shifts manifest as a substantially higher effective barrier, inherently resulting in a lower α_{H} value. In this high-barrier regime, the exponential term becomes exceedingly sensitive to temperature fluctuations. The gain in thermal energy ($k_B T$) thus dominates the kinetic evolution, leading to the drastic, monotonic increase in α_{H} observed at elevated temperatures.

In contrast to α, Γ decreases monotonically with temperature and spans a wide range from 10^{14} to 10^{17} across the investigated CVD temperature window. This decrease in Γ is dominated by the rapid increase in F_{eff} at higher temperatures.

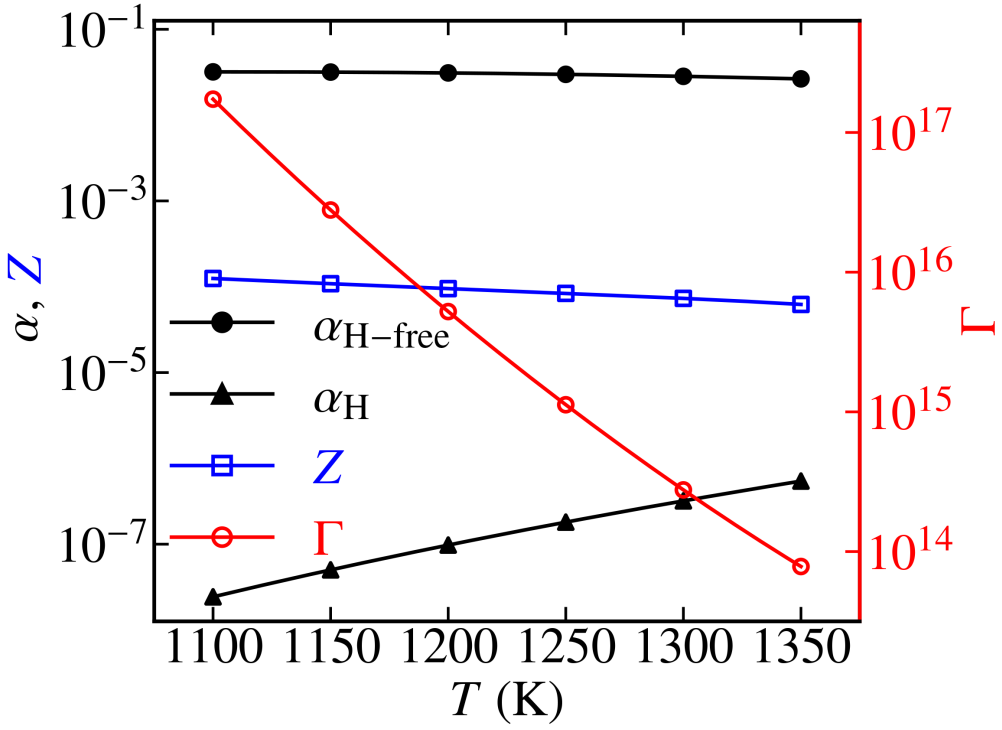


Figure 4: The estimated values of parameters α, Γ and Z as a function of temperature for $p_{H_2} = 0.01$ bar and $w = 100$.

The dependence of Γ on gas partial pressures at different temperatures is further given in Fig. S11, where a wider range of $t = P_{H_2}/P^{\ominus}$ and $w = P_{H_2}/P_{CH_4}$ is considered. Across all investigated conditions, Γ decreases with increasing temperature but increases with an increase in either t or w, corresponding to higher P_{H_2} or lower P_{CH_4}, respectively.

The dependence of Z on growth conditions is evaluated via Eqs. (5) and (9). At fixed P_{H_2}, Z decreases slightly with increasing temperature, as shown by the blue curve in Fig. 4. Although both ν_1 and z_{eff} increase with temperature, the stronger enhancement of ν_1 relative to z_{eff} leads to an overall reduction in Z. In contrast, increasing in hydrogen partial pressure promotes chemical desorption, thereby yielding higher values for both z_{eff} and Z, as shown in Fig. S12. Consequently, while thermal strain influences graphene growth through concurrent modifications of kinetic parameters, chemical desorption primarily affects the growth behavior through the evolution of the kinetic parameter Z. With the temperature dependence of these parameters established, we next turn to the discussion of the generalized growth phase diagram.

3.3.2. Generalized Phase diagram

By adopting $\sigma_{i^*} = 2$, $\sigma_s = 10$, and $\Theta_c = 0.2$ as in our previous report [35], the phase diagram is constructed via Eq. (14) as a function of the dimensionless parameters α and Γ. Figures 5(a) and (b) show the phase diagrams at $T = 1300$ K for $Z = 0$ and $Z \neq 0$, respectively, both incorporating the effects of thermal-expansion-induced strain. Here, phase boundaries corresponding to different critical nucleus sizes i^* are explicitly depicted. A given set of CVD conditions maps onto a corresponding supersaturation and strain state, thereby selecting the relevant i^* regime and its phase boundaries.

The generalized phase diagram reveals a qualitatively different strain response between the $i^* = 1$ and $i^* > 1$ growth regimes. As shown in Fig. 5(a), the phase boundary between BLG and SLG growth deviates significantly from our previous results once temperature-dependent effects are incorporated. For $i^* = 1$, the BLG growth regime contracts slightly. Since the cluster formation energy vanishes in this limit, the temperature dependence of Eq. (14) arises solely through the parameter λ. Thermal strain increases ΔG_4 while decreasing ΔG_1, thereby reducing λ and shrinking the BLG region. In contrast, for $i^* > 1$, the strain-dependent formation energies F_{gap} and F_{surf} become active simultaneously. Although the increase in F_{gap} suppresses second-layer nucleation, the concurrent increase in F_{surf} lowers the island density θ_{isl} and increases the average island separation L, which favors second-layer growth. The competition between these two effects ultimately expands the BLG regime, particularly for larger critical nucleus sizes (e.g., $i^* = 6$), representing a notable deviation from the strain-free case.

When chemical desorption is incorporated, the phase diagram is presented in Fig. 5(b) for $T = 1300$ K and $P_{H_2} = 0.01$ bar. In addition to the coefficients B_{i^*} and C_{i^*}, the phase boundary now depends explicitly on the factor $[\theta_{isl}/(\theta_{isl} + Z)]^{i^*}$ in Eq. (14), which couples the second-layer nucleation number to both the island coverage θ_{isl} and the chemical desorption strength Z. In the low-Γ regime corresponding to high deposition rates, θ_{isl} remains sufficiently large such that the Z-dependent factor approaches unity. The resulting phase boundary therefore remains close to the $Z = 0$ limit. In contrast, for large Γ, the reduced island coverage enhances the influence of chemical desorption, and the Z-dependent factor suppresses the second-layer nucleation number I_i, thereby inhibiting BLG formation. Consequently, the phase boundary bends downward in the high-Γ regime, leading to a reduced BLG region. A notable exception occurs for $i^* = 1$, where the term $[\theta_{isl}/(\theta_{isl} + Z)]$ is insufficient to offset the favorable changes in C_{i^*} for BLG growth. As a result, the BLG domain becomes slightly expanded for large-Γ in Fig. 5(b).

The temperature dependence of the phase boundaries is further examined in Figs. S13 and S14 for the cases of

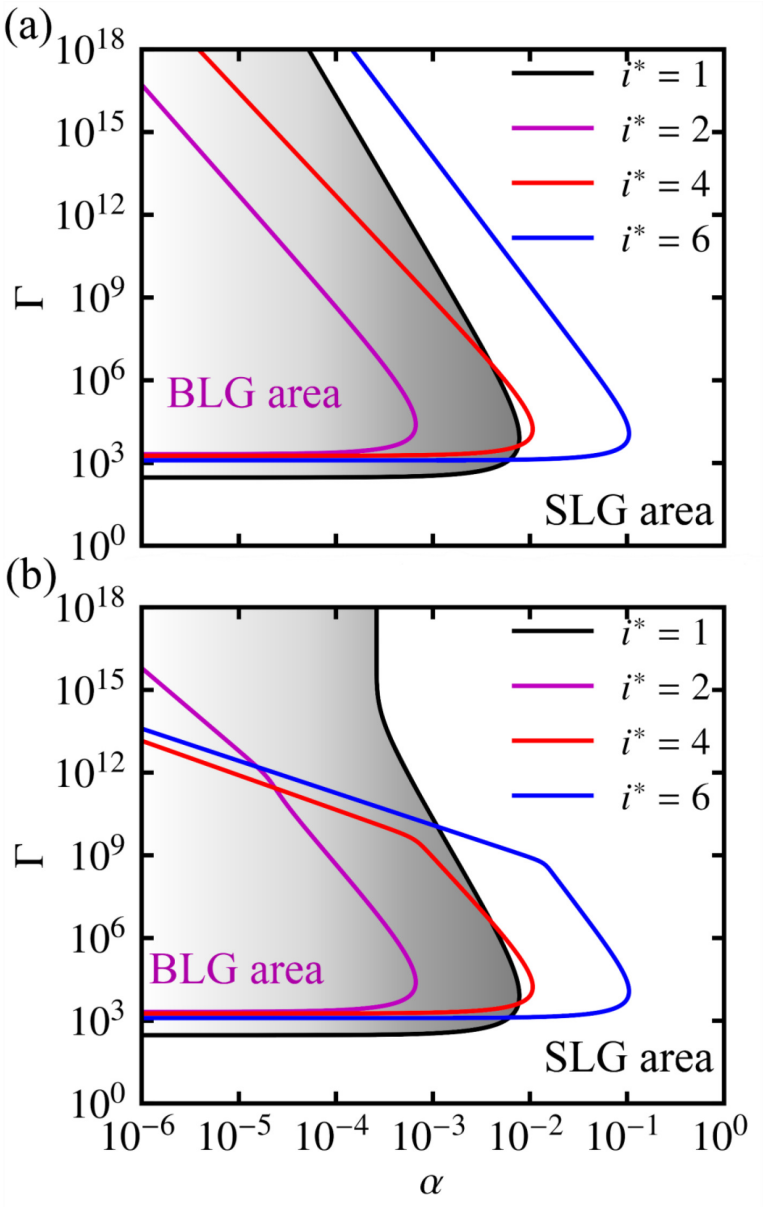


Figure 5: Growth mode diagrams of graphene on Cu(111) at T = 1300 K, incorporating thermal activation and substrate thermal expansion. The chemical desorption of carbon is (a) excluded ($Z = 0$) and (b) included ($Z \neq 0$).

$Z = 0$ and $Z \neq 0$, respectively. In the absence of chemical desorption ($Z = 0$), the BLG region contracts slightly with increasing temperature for $i^* = 1$. Since $\Delta F = 0$ in this limit, the temperature dependence arises primarily from the variation of λ. In contrast, for $i^* > 1$, the BLG growth window expands at elevated temperatures. This behavior originates from the competing strain-induced variations of ΔF_{surf} and ΔF_{gap}. Although increasing temperature generally suppresses nucleation on both layers, the second-layer nucleation barrier exhibits a weaker temperature dependence than that of the first layer. Consequently, the relative suppression of first-layer nucleation becomes more pronounced, ultimately favoring BLG growth and expanding the BLG regime in phase space. For the $Z \neq 0$ case, chemical desorption primarily modifies the phase boundary in the high-Γ regime through the Z-dependent factor discussed above without altering the fundamental temperature-dependent evolution of the growth modes. The resulting trends therefore remain consistent with the $Z = 0$ case: the BLG regime contracts slightly for $i^* = 1$ but expands substantially for $i^* > 1$ as temperature increases.

3.3.3. Strategies for Bilayer Synthesis

Although the phase diagram is formulated in terms of the dimensionless parameters α and Γ, these quantities map directly onto experimentally tunable parameters, including gas partial pressures and temperature. As summarized in Fig. S11, Γ typically spans the range from 10^{12} to 10^{20} under standard CVD conditions, indicating that most experiments operate within the large-Γ regime of the generalized phase diagram. Experimentally, the hydrogen partial pressure provides an effective approach for tuning the parameter α through hydrogen-dependent edge kinetics. Low P_{H_2} stabilizes H-free graphene edges and therefore maintains relatively large α, favoring SLG expansion. In contrast, increasing P_{H_2} promotes hydrogen termination of the graphene edge, reduces α, and consequently facilitates BLG nucleation. More generally, these results demonstrate that layer selectivity can be achieved by mapping experimental conditions (temperature and chemical environment) onto the (α,Γ) parameter space.

More importantly, the generalized phase diagrams suggest that elevated growth temperatures can move the system deeper into the BLG-favorable region of phase space for $i^* > 1$. This theoretical framework therefore provides a natural mechanistic interpretation for several experimental observations. For instance, Celebi *et al.* reported that the secondary graphene flake area increases with growth temperature [65]. Fabiane *et al.* further observed that BLG synthesized at relatively low temperature ($\sim 780\,^\circ$C) exhibits substantial structural disorder, whereas growth at higher temperatures ($\sim$ 956–973 $^\circ$C) predominantly yields high-quality AB-stacked bilayer islands [66]. More broadly, experiments on Cu-catalyzed CVD systems consistently indicate that low-temperature growth strongly favors single-layer graphene formation [67,68]. These experimental trends are fully consistent with the temperature-dependent expansion of the BLG regime predicted by our generalized phase diagrams. Given that this BLG growth window narrows at reduced temperatures, approaches such as nucleation-density engineering or the Cu-pocket method may provide viable pathways for overcoming these kinetic limitations.

Beyond temperature-driven strain, epitaxial strain introduced during substrate preparation provides an additional route for tuning graphene growth behavior. Epitaxial tensile strain exerts a similar influence as thermal expansion, expanding the BLG growth window for $i^* > 1$. This result provides a natural explanation for the enhanced bilayer yield frequently observed on heteroepitaxial substrates. For instance, the lattice mismatch between sapphire and $(\sqrt{3}\times\sqrt{3})$ Cu(111) induces an intrinsic tensile strain of approximately 6% in the Cu film [64,69–71]. As discussed in Sec. 3.3.2, such tensile strain, whether originating from epitaxial mismatch or further enhanced by thermal expansion, shifts the operating point deeper into the BLG regime of the generalized phase diagram. This cooperative effect is particularly evident in CuNi(111)/sapphire systems [64,72]. Furthermore, this framework is consistent with the experimental realization of nearly 100% AB-stacked BLG single crystals on ultraflat Cu(111)/sapphire substrates [73].

Collectively, temperature tuning and epitaxial strain engineering provide complementary approaches for controlling graphene layer number during CVD growth. To further assess the experimental relevance of the generalized phase diagrams, representative experimental observations are compared with the corresponding growth-mode predictions in Table S4. Although the present framework does not predict absolute island densities or final BLG yields, the experimentally observed responses to temperature, hydrogen environment, and epitaxial substrate conditions are qualitatively consistent with the predicted shifts between the SLG- and BLG-favorable regimes. These comparisons support the utility of the phase diagrams for identifying growth conditions favorable for layer-selective graphene synthesis. Combined with the strategies proposed in our previous work [35], the present framework establishes a versatile parameter space for synthesizing high-quality bilayer graphene.

4. Conclusions

In summary, we establish a generalized kinetic framework for graphene CVD growth on Cu substrates by incorporating strain-modulated surface kinetics and chemical desorption into our previous phase-diagram model. Through first-principles calculations and rate-equation analysis, we demonstrate that the complex CVD process is governed by the competition between first-layer lateral expansion and second-layer nucleation, which is regulated by the kinetic parameters α, Γ, and Z. Crucially, tensile strain alters this competitive balance. It leaves the $i^* = 1$ regime weakly affected but expands the BLG growth window for $i^* > 1$ by shifting the nucleation energetics of both layers. In contrast, chemical desorption acts as a kinetic suppression mechanism, with the parameter Z inhibiting BLG formation in the high-Γ regime for $i^* > 1$. These findings establish a generalized phase diagram directly connected to experimental variables, including temperature, hydrogen partial pressure, and epitaxial strain. Future extensions of this framework will consider more complex growth mechanisms, such as hydrogen-stabilized carbon intermediates and reconstruction-mediated sunk growth, to further broaden its applicability. Beyond explaining observed experimental trends, this framework provides a predictive and experimentally navigable guide for the rational synthesis of high-quality bilayer graphene and other two-dimensional materials.

Appendix A: Supplementary Information

Please see Supplementary Information file.

Data availability statement

The data that support the findings of this study are available from the corresponding author upon reasonable request.

Acknowledgement

The numerical calculations were carried out at the High Performance Computing Center of Nanjing University. This work was supported by the National Natural Science Foundation of China (Grants No. 12188101, No. 12274211) and Fundamental and Interdisciplinary Disciplines Breakthrough Plan of the Ministry of Education of China (Grant No. JYB2025XDXM409).

References

[1] Novoselov K S, Geim A K, Morozov S V, Jiang D, Zhang Y, Dubonos S V, Grigorieva I V and Firsov A A 2004 *Science* **306** 666–669

[2] Kim K S, Zhao Y, Jang H, Lee S Y, Kim J M, Kim K S, Ahn J H, Kim P, Choi J Y and Hong B H 2009 *Nature* **457** 706–710

[3] Shen J, Zhu Y, Yang X and Li C 2012 *Chem. Commun.* **48**(31) 3686–3699

[4] Novoselov K S, Jiang Z, Zhang Y, Morozov S V, Stormer H L, Zeitler U, Maan J C, Boebinger G S, Kim P and Geim A K 2007 *Science* **315** 1379–1379

[5] Balandin A A 2011 *Nat. Mater.* **10** 569–581

[6] Lee C, Wei X, Kysar J W and Hone J 2008 *Science* **321** 385–388

[7] Xia F, Farmer D B, Lin Y m and Avouris P 2010 *Nano Lett.* **10** 715–718

[8] Castro E V, Novoselov K S, Morozov S V, Peres N M R, dos Santos J M B L, Nilsson J, Guinea F, Geim A K and Neto A H C 2007 *Phys. Rev. Lett.* **99**(21) 216802

[9] Island J O, Cui X, Lewandowski C, Khoo J Y, Spanton E M, Zhou H, Rhodes D, Hone J C, Taniguchi T, Watanabe K, Levitov L S, Zaletel M P and Young A F 2019 *Nature* **571** 85–89

[10] Cao Y, Fatemi V, Demir A, Fang S, Tomarken S L, Luo J Y, Sanchez-Yamagishi J D, Watanabe K, Taniguchi T, Kaxiras E, Ashoori R C and Jarillo-Herrero P 2018 *Nature* **556** 80–84

[11] Cao Y, Fatemi V, Fang S, Watanabe K, Taniguchi T, Kaxiras E and Jarillo-Herrero P 2018 *Nature* **556** 43–50

[12] Lee H C, Liu W W, Chai S P, Mohamed A R, Lai C W, Khe C S, Voon C, Hashim U and Hidayah N 2016 *Procedia Chemistry* **19** 916–921

[13] Novoselov K S, Fal′ko V I, Colombo L, Gellert P R, Schwab M G and Kim K 2012 *Nature* **490** 192–200

[14] Yagi R, Hirahara T, Ebisuoka R, Nakasuga T, Tajima S, Watanabe K and Taniguchi T 2018 *Sci. Rep.* **8** 13018

[15] Nagashio K, Nishimura T, Kita K and Toriumi A 2009 *Appl. Phys. Express* **2** 025003

[16] Gajewski G and Pao C W 2011 *J. Chem. Phys.* **135** 064707

[17] He Y, Wang H, Jiang S and Mo Y 2019 *Comput. Mater. Sci* **168** 17–24

[18] Li K, He C, Jiao M, Wang Y and Wu Z 2014 *Carbon* **74** 255–265

[19] Zhang W, Wu P, Li Z and Yang J 2011 *J. Phys. Chem. C* **115** 17782–17787

[20] Wang X, Yuan Q, Li J and Ding F 2017 *Nanoscale* **9**(32) 11584–11589

[21] Ma T, Ren W, Zhang X, Liu Z, Gao Y, Yin L C, Ma X L, Ding F and Cheng H M 2013 *Proc. Natl. Acad. Sci. U.S.A.* **110** 20386–91

[22] Qiu Z, Li P, Li Z and Yang J 2018 *Acc. Chem. Res.* **51** 728–735

[23] Li P and Li Z 2020 *J. Phys. Chem. C* **124** 16233–16247

[24] Cheng T, Sun L, Liu Z, Ding F and Liu Z 2021 *APL Mater.* **9** 060906

[25] Li P, Li Z and Yang J 2017 *J. Phys. Chem. C* **121** 25949–25955

[26] Chen S, Gao J, Srinivasan B M, Zhang G, Sorkin V, Hariharaputran R and Zhang Y W 2019 *Carbon* **146** 399–405

[27] Kong X, Zhuang J, Zhu L and Ding F 2021 *npj Comput. Mater.* **7** 14

[28] Zhang D, Yi P, Lai X, Peng L and Li H 2024 *Nat. Commun.* **15** 344

[29] Chen W, Cui P, Zhu W, Kaxiras E, Gao Y and Zhang Z 2015 *Phys. Rev. B* **91**(4) 045408

[30] Hong H C, Ryu J I and Lee H C 2023 *Nanomaterials* **13** 2217

[31] Xue R, Abidi I H and Luo Z 2017 *Funct. Mater. Lett.* **10** 1730003

[32] Sun L, Wang Z, Wang Y, Zhao L, Li Y, Chen B, Huang S, Zhang S, Wang W, Pei D, Fang H, Zhong S, Liu H, Zhang J, Tong L, Chen Y, Li Z, Rummeli M H, Novoselov K S, Peng H, Lin L and Liu Z 2021 *Nat. Commun.* **12** 2391

[33] Li Q, Chou H, Zhong J H, Liu J Y, Dolocan A, Zhang J, Zhou Y, Ruoff R S, Chen S and Cai W 2013 *Nano Lett.* **13** 486–490

[34] Nie S, Wu W, Xing S, Yu Q, Bao J, Pei S s and McCarty K F 2012 *New J. Phys.* **14** 093028

[35] Wang T, Zheng J, Wei X and Shu D 2025 *Phys. Rev. Mater.* **9**(2) L021001

[36] Wang K and Reeber R 1996 *High Temp. Mater. Sci.* **35** 181–186

[37] Mondal A, Wijzenbroek M, Bonfanti M, Díaz C and Kroes G J 2013 *J. Phys. Chem. A* **117** 8770–8781

[38] Marashdeh A, Casolo S, Sementa L, Zacharias H and Kroes G J 2013 *J. Phys. Chem. C* **117** 8851–8863

[39] Dong Y, Guo S, Mao H, Xu C, Xie Y, Cheng C, Mao X, Deng J, Pan G and Sun J 2019 *Nanomaterials* **9** 1633

[40] Vlassiouk I, Regmi M, Fulvio P, Dai S, Datskos P, Eres G and Smirnov S 2011 *ACS Nano* **5** 6069–6076

[41] Sun X, Lou S, Wang W, Liu X, Sun X, Song Y, Yang W and Liu Z 2024 *Nano Res.* **17** 9284–9292

[42] Leidinger P, Kratky T and Günther S 2023 *J. Phys. Chem. C* **127** 8136–8147

[43] Zhao P, Cheng Y, Zhao D, Yin K, Zhang X, Song M, Yin S, Song Y, Wang P, Wang M, Xia Y and Wang H 2016 *Nanoscale* **8** 7646–7653

[44] Mitchell I and Page A 2018 *Carbon* **128** 215–223

[45] Dai X, Mitchell I, Kim S, An H and Ding F 2022 *Carbon* **199** 233–240

[46] Xu Z, Zhao G, Qiu L, Zhang X, Qiao G and Ding F 2020 *npj Comput. Mater.* **6** 14

[47] Chen B, Zeng X, Liu Z, Dong W, Pei D, Wang H, Dong Y, Wu C, Gao X, Xiao H, Gao H, Jia H, Yuan A, Du J, Chen H, Liu H, Tan C, Yin J, Liu Z, Liu L, Gao P, Novoselov K S, Peng H, Li Z, Sun L and Liu Z 2025 *Nat. Commun.* **16** 5490

[48] Perdew J P, Burke K and Ernzerhof M 1996 *Phys. Rev. Lett.* **77**(18) 3865–3868

[49] Kresse G and Furthmüller J 1996 *Comput. Mater. Sci* **6** 15–50

[50] Kresse G and Furthmüller J 1996 *Phys. Rev. B* **54**(16) 11169–11186

[51] Blöchl P E 1994 *Phys. Rev. B* **50**(24) 17953–17979

[52] Bučko T, Hafner J, Lebègue S and Ángyán J G 2010 *J. Phys. Chem. A* **114** 11814–11824

[53] Methfessel M and Paxton A T 1989 *Phys. Rev. B* **40**(6) 3616–3621

[54] Henkelman G, Uberuaga B P and Jónsson H 2000 *J. Chem. Phys.* **113** 9901–9904

[55] Leidinger P and Günther S 2021 *J. Phys. Chem. C* **125** 12663–12671

[56] Huet B and Raskin J P 2017 *Chem. Mater.* **29** 3431–3440

[57] Lee S, Lee K and Zhong Z 2010 *Nano Lett.* **10** 4702–4707

[58] Cho S Y, Kim M S, Kim M, Kim K J, Kim H M, Lee D J, Lee S H and Kim K B 2015 *Nanoscale* **7**(30) 12820–12827

[59] Zhong L, Li J, Li Y, Lu H, Du H, Gan L, Xu C, Chiang S W and Kang F 2016 *The Journal of Physical Chemistry C* **120** 23239–23245

[60] Van Wesep R G, Chen H, Zhu W and Zhang Z 2011 *The Journal of Chemical Physics* **134** 171105

[61] Walton D 1962 *J. Chem. Phys.* **37** 2182–2188

[62] Venables J A 1973 *Philos. Mag.* **27** 697–738

[63] Venables J A, Spiller G D T and Hanbucken M 1984 *Rep. Prog. Phys.* **47** 399–459

[64] Tang J, Wang Y, Ma Y, Gao X, Gao X, Li N, Wang Y, Zhang S, Zheng L, Deng B, Yan R, Cao Y, Zhang R, Tong L, Zhang J, Gao P, Liu Z, Wei X, Liu H and Peng H 2023 *Nano Res.* **16** 10684–10689

[65] Celebi K, Cole M T, Choi J W, Wyczisk F, Legagneux P, Rupesinghe N, Robertson J, Teo K B and Park H G 2013 *Nano Lett.* **13** 967–74

[66] Fabiane M, Madito M J, Bello A and Manyala N 2017 *J. Raman Spectrosc.* **48** 639–646

[67] Weatherup R S, Dlubak B and Hofmann S 2012 *ACS Nano* **6** 9996–10003

[68] Mehdipour H and Ostrikov K K 2012 *ACS Nano* **6** 10276–10286

[69] Li J, Chen M, Samad A, Dong H, Ray A, Zhang J, Jiang X, Schwingenschlgl U, Domke J, Chen C, Han Y, Fritz T, Ruoff R S, Tian B and Zhang X 2022 *Nat. Mater.* **21** 740–747

[70] Zhang X, Wu T, Jiang Q, Wang H, Zhu H, Chen Z, Jiang R, Niu T, Li Z, Zhang Y, Qiu Z, Yu G, Li A, Qiao S, Wang H, Yu Q and Xie X 2019 *Small* **15** e1805395

[71] Deng B, Pang Z, Chen S, Li X, Meng C, Li J, Liu M, Wu J, Qi Y, Dang W, Yang H, Zhang Y, Zhang J, Kang N, Xu H, Fu Q, Qiu X, Gao P, Wei Y, Liu Z and Peng H 2017 *ACS Nano* **11** 12337–12345

[72] Takesaki Y, Kawahara K, Hibino H, Okada S, Tsuji M and Ago H 2016 *Chem. Mater.* **28** 4583–4592

[73] Zhang J, Liu X, Zhang M, Zhang R, Ta H Q, Sun J, Wang W, Zhu W, Fang T, Jia K, Sun X, Zhang X, Zhu Y, Shao J, Liu Y, Gao X, Yang Q, Sun L, Li Q, Liang F, Chen H, Zheng L, Wang F, Yin W, Wei X, Yin J, Gemming T, Rummeli M H, Liu H, Peng H, Lin L and Liu Z 2023 *Nat. Commun.* **14** 3199